# Breaks in interstellar spectra of positrons and electrons derived from time-dependent AMS data

Andrea Vittino,[1] Philipp Mertsch,[1] Henning Gast,[2] and Stefan Schael[2]
[1]*Institute for Theoretical Particle Physics and Cosmology (TTK), RWTH Aachen University, 52056 Aachen, Germany*
[2]*I. Physics Institute and JARA-FAME, RWTH Aachen University, 52056 Aachen, Germany*

(Received 11 April 2019; published 9 August 2019)

Until fairly recently, it was widely accepted that local cosmic-ray spectra were largely featureless power laws, containing limited information about their acceleration and transport. This viewpoint is currently being revised in light of evidence for a variety of spectral breaks in the fluxes of cosmic-ray nuclei. Here, we focus on cosmic-ray electrons and positrons which at the highest energies must be of local origin due to strong radiative losses. We consider a pure diffusion model for their Galactic transport and determine its free parameters by fitting data in a wide energy range: measurements of the interstellar spectrum by Voyager at mega-electron-volt energies, radio synchrotron data (sensitive to giga-electron-volt electrons and positrons), and local observations by AMS up to approximately 1 TeV. For the first time, we also model the time-dependent fluxes of cosmic-ray electrons and positrons at giga-electron-volt energies recently presented by AMS, treating solar modulation in a simple extension of the widely used force-field approximation. We are able to reproduce all the available measurements to date. Our model of the interstellar spectrum of cosmic-ray electrons and positrons requires the presence of a number of spectral breaks, both in the source spectra and the diffusion coefficients. While we remain agnostic as to the origin of these spectral breaks, their presence will inform future models of the microphysics of cosmic-ray acceleration and transport.

DOI: 10.1103/PhysRevD.100.043007

## I. INTRODUCTION

The last decades have witnessed an impressive effort aimed at understanding the acceleration and the transport of Galactic cosmic rays (CRs). On the observational side, a large number of experiments have presented measurements of local fluxes of various CR species and their combined anisotropy. In addition, measurements of the diffuse gamma-ray flux contain information about the CR fluxes in other regions of the Galaxy. The wealth of accurate and diverse data has challenged our understanding of CR origin and propagation. In particular, the long-held wisdom that CR spectra are featureless power laws from giga-electron-volt to peta-electron-volt energies had to be revised in the light of a number of spectral breaks observed, most prominently the "discrepant hardening" in nuclei fluxes at rigidities of a few hundred gigavolts [1–5]. On the modeling side, this requires modifications of the underlying assumptions, in particular on the shapes of source spectra and the rigidity dependence of the Galactic diffusion coefficient.

CR electrons and positrons are of central importance in investigating the origin of CRs in that at the highest energies they must be necessarily of local origin. For example, in the usually assumed radiation fields (cf., e.g., Ref. [6]), electrons of 1 TeV cool in approximately $3 \times 10^5$ yr, which limits their distances to approximately 300 pc. (Here, we have assumed a diffusion coefficient of $10^{29}$ cm$^2$ s$^{-1}$.) Specifically, spectral features at hundreds of giga-electron-volts or higher energies can be related to individual sources of CR electrons and positrons. In addition, CR electrons and positrons in other regions of the Galaxy contribute to the diffuse emission at radio/microwave and gamma-ray wavelengths by synchrotron emission and inverse Compton scattering, respectively. Understanding the local fluxes is imperative for any global model of CR electrons and positrons. Finally, CR positrons have received heightened attention as a probe for dark matter annihilation or decay. The fluxes of CR electrons and positrons from astrophysical sources constitute an irreducible background for any search of exotic signatures such that precise predictions are required.

In CR electrons and positrons, two features have attracted the most attention over the last decade. First, the positron fraction, i.e., the ratio of the positron flux to the sum of electron and positron fluxes, is rising above approximately 7 GeV. The existence of such a rise, which was already hinted at in the 1–50 GeV energy range by the HEAT observations in 1994 [7,8], was proven by the PAMELA orbital observatory [9] and later confirmed by AMS at an unprecedented level of precision [4]. Over the years, this excess of high-energy positrons has attracted several

 

interpretations mostly in terms of astrophysical mechanisms such as the emission from pulsar wind nebulae [10,11] or the diffusive shock acceleration of positrons produced in spallation reactions occurring inside the shock region of one or more supernova remnants (SNRs) [12,13]. Numerous interpretations of this anomaly in terms of dark matter annihilation or decay have also been put forward [14,15], even if it has been shown that such interpretations can be in strong contention with the constraints that are derived from other dark matter indirect detection channels [16]. Secondly, a spectral softening was observed in the sum of electron and positron fluxes at approximately 1 TeV by H.E.S.S. observations [17,18] and recently confirmed by DAMPE [19]. Very recently, AMS reported a spectral cutoff in the positrons around 300 GeV [20], notably at significantly smaller energies than the break in the all-electron spectrum.

At energies below a few tens of giga-electron-volts, studies of the interstellar spectra are hampered by solar modulation, that is the energy losses and flux suppression due to the interaction of CRs with the solar wind and its frozen-in magnetic field. (See Ref. [21] for a review). This modulation is periodic with a primary period of 11 years. Until recently, the statistics of the experimental data was such that only CR spectra averaged over significant fractions of the 11 year period and therefore only studies of the average properties of solar modulation were possible. These time-averaged data could be reasonably well described by the simple and popular force-field model. Recently, the substantial increase in the number of events collected by the detectors has made time-dependent measurements of CR spectra possible. Time-dependent lepton spectra have been released by PAMELA [22,23] and AMS [24]. In particular, Ref. [22] reports the measurement performed by PAMELA of the electron flux in the [70 MeV–50 GeV] energy range, binned in seven time bins (of around six months each) that cover the solar minimum from July 2006 to December 2009. PAMELA has also presented the positron-to-electron ratio in the [500 MeV–5 GeV] energy range for 35 time intervals (of around three months each) between July 2006 and December 2015 [23]. AMS has presented the electron flux, the positron flux, and the positron-to-electron ratio measured in the [1 GeV–50 GeV] energy range and in the time period from June 2011 to April 2017, binned in time intervals with a duration of one Bartels rotation each [24].

The study of solar modulation and modeling of the interstellar spectra benefits not only from these new time-dependent measurements but also from the first direct measurements in the interstellar medium. Specifically, the Voyager I spacecraft, launched in 1977, transited the heliopause in 2012 and entered into interstellar space [25]. It should be mentioned, in any case, that the Voyager measurements are at significantly lower energies than those at the Earth's position such that the effect of solar modulation cannot be estimated without an extrapolation or, better, modeling of the spectra.

The aim of this paper is to model the electron and positron local interstellar spectra (LIS) over a wide energy range from tens of mega-electron-volts to approximately tera-electron-volts. Our model will contain a number of spectral breaks in the source spectra and in the rigidity dependence of the diffusion coefficient. To this end, we will exploit a variety of complementary experimental datasets. We will emphasize which dataset requires the introduction of which spectral break. Our analysis will benefit from the recent time-dependent measurements of the electron and positron fluxes performed by AMS [24]. We will illustrate how the effect of solar modulation on these fluxes can be described to a very good extent within the framework of a simple analytical extension of the force-field approximation.

The paper is organized as follows. In Sec. II, we illustrate the main features that characterize our implementation of the acceleration and transport of CR electrons and positrons. In Sec. III, we describe the setup of the different analyses that we perform, and we discuss our results. Then, in Sec. IV, we summarize our findings and provide our conclusions.

## II. METHOD

### A. CR sources

CR electrons and positrons can be of either primary or secondary origin. Primary CRs are those particles that undergo acceleration in astrophysical sources. Primary electrons are expected to be accelerated by SNRs through diffusive shock acceleration. The number of CRs of a given species injected by SNRs into the interstellar medium (ISM) per unit time, volume, and energy is described by a source term that can be expressed as

$$\mathcal{Q}_{\rm SNR} = \mathcal{Q}_0 f(r,z) g(\mathcal{R}), \tag{1}$$

where we have made the standard assumption that the rigidity and spatial dependence can be factorized. The rigidity dependence is defined by the function $g(\mathcal{R})$, which we assume to be a power law, possibly with a number of breaks, as will be illustrated in greater detail in Sec. III for the different steps of our analysis. The function $f(r,z)$, which describes the spatial dependence of the SNR source term, is assumed to be the one proposed by Ref. [26].[1] Lastly, the normalization factor $\mathcal{Q}_0$ takes into account the rate of supernova explosions and the luminosity that SNRs inject into the ISM in the form of CRs.

As mentioned above, for the rise in the positron fraction, several interpretations have been put forward. In this paper,

[1]We have verified that the use of the source profile proposed in Ref. [27] gives identical results to the ones presented in Sec. III. On the other hand, the profile proposed in Ref. [28], which is significantly different than the ones in Refs. [26] and [27], results in a slightly different $e^{\pm}$ spectrum in the mega-electron-volt range and therefore would require different values for the parameters that will be introduced to fit Voyager data in Sec. III C.

we take a model-independent viewpoint and assume this extra component of high-energy electrons and positrons to have a spatial dependence that traces the one of SNRs and a rigidity dependence that can be expressed as a power law with an exponential cutoff:

$$\mathcal{Q}_{\rm extra} = N_x \left(\frac{\mathcal{R}}{\mathcal{R}_0}\right)^{-\Gamma_x} \exp\left(-\frac{\mathcal{R}}{\mathcal{R}_{\rm cut}}\right) f(r,z). \quad (2)$$

Such a spectrum is compatible with models that describe the acceleration of electrons and positrons in the magnetosphere of pulsars (see the discussion in Ref. [11]) as well as with models that describe the acceleration of secondary positrons in SNRs (as detailed in Ref. [13]). In all our investigations, we adopt $\mathcal{R}_{\rm cut} = 600$ GV. We assume $\mathcal{Q}_{\rm extra}$ to be a charge-symmetric source term, in the sense that the electron and positron spectra injected into the ISM by the extra source are identical. This assumption is not perfectly consistent with our model-independent take on the extra term. Indeed, while pulsars are expected to be charge-symmetric sources of CR leptons, other sources invoked as interpretations to the rising positron fraction may not be. As an example, if one assumes this extra source to be SNRs accelerating secondaries produced in spallation reactions, such a mechanism will produce slightly more positrons than electrons (as a consequence of charge conservation in proton-proton collisions). If we were to fix the normalization of the extra source by fitting to the positron flux, the small charge asymmetry would have a negligible impact on the electron flux as typically high-energy electrons are dominated by the SNR component described by $\mathcal{Q}_{\rm SNR}$. In any case, one has to consider that within the present experimental precision a charge-symmetric source term can be neither confirmed nor excluded.

Secondary electrons and positrons are produced by the interaction of primary CRs (mostly proton, denoted here with p, and He nuclei) scattering off the hydrogen and helium nuclei of the ISM. We describe this process with the source term

$$\mathcal{Q}_{e^\pm}(\mathcal{R},\vec{x}) = 4\pi \sum_{i={\rm p,He}} \sum_{j={\rm H,He}} n_j \int dE_i \Phi_i(\mathcal{R},\vec{x}) \frac{d\sigma}{d\mathcal{R}}(i+j\to e^\pm + X), \quad (3)$$

where $\frac{d\sigma}{d\mathcal{R}}(i+j\to e^\pm+X)$ represents the differential inclusive cross section for the production of electrons and positrons in $ij$ reactions; for the $pp$ case, we take the parametrization proposed in Refs. [29,30], while for the processes involving He, as a projectile or as a target, we adopt the rescaling of the $pp$ cross section obtained by following the prescriptions given in Ref. [31]. The quantity $n_j$ represents the density of the target species $j$, which is taken from the model discussed in Ref. [32], while $\Phi_i(\mathcal{R},\vec{x})$ is the flux of the primary CR species $i$.

### B. Galactic propagation setup

CRs propagate across the diffusive halo of the Galaxy, which we assume here to be a cylinder of half-height $H = 4$ kpc and radius $R = 20$ kpc. The propagation is characterized by the interplay between several processes, and it is typically described in terms of a transport equation which models the time evolution of the CR density per unit momentum $\Psi(\vec{r},p,t)$, which is related to the CR flux $\Phi$ by the relation $\Phi = v/(4\pi)\Psi$, with $v$ being the CR velocity. In full generality, the transport equation can be written as [33,34]

$$\begin{aligned}\frac{\partial\Psi(\vec{r},p,t)}{\partial t} &= \mathcal{Q}(\vec{r},p,t) + \vec{\nabla}\cdot(D_{xx}\vec{\nabla}\Psi(\vec{r},p,t) - \vec{V}_c\Psi(\vec{r},p,t)) \\ &+ \frac{\partial}{\partial p}p^2 D_{pp}\frac{\partial}{\partial p}\frac{1}{p^2}\Psi(\vec{r},p,t) \\ &- \frac{\partial}{\partial p}\left[\dot{p} - \frac{p}{3}(\vec{\nabla}\cdot\vec{V}_c)\Psi(r,\vec{p},t)\right] \\ &- \Psi(\vec{r},p,t)\left(\frac{1}{\tau_f} - \frac{1}{\tau_r}\right). \end{aligned} \quad (4)$$

We adopt the free-escape boundary condition, $\psi(z=\pm H)=0$.

As is customary, we have written the above equation in terms of the CR momentum per nucleon $p$, related to the rigidity $\mathcal{R}$ by the relation $p = (Z/A)\mathcal{R}$, with $A$ and $Z$ being, respectively, the mass and atomic number of the CR species under consideration. The terms on the right-hand side of Eq. (4) describe, respectively, the CR source terms (as described in the previous paragraph), spatial diffusion, convection (with the velocity of the convective wind being $\vec{V}_c$), diffusive reacceleration, energy losses, and (in the fourth line) nuclear fragmentation and radioactive decays. These two processes are characterized, respectively, by the timescales $\tau_f$ and $\tau_r$ (with $\tau_r$ being the lifetime of the CR species under consideration). The terms in the third line are to be included only when treating CR nuclei, as it is in the case discussed in Sec. III A.

In this paper, we consider a simplified form of the transport equation, which we use to model the transport of all CR species and which refers to a scenario where both diffusive reacceleration and convection are neglected. Our transport equations, which we solve with the publicly available DRAGON code [35], are therefore

$$\frac{\partial\Psi}{\partial t} = \begin{cases} \mathcal{Q} + \vec{\nabla}\cdot D_{xx}\vec{\nabla}\Psi - \frac{\partial}{\partial p}\dot{p} - \frac{1}{\tau_f}\Psi - \frac{1}{\tau_r}\Psi & \text{CR nuclei,} \\ \mathcal{Q} + \vec{\nabla}\cdot D_{xx}\vec{\nabla}\Psi - \frac{\partial}{\partial p}\dot{p} & \text{CR leptons.} \end{cases} \quad (5)$$

In the following, we only consider steady-state solutions, i.e., $\partial\Psi/\partial t \equiv 0$.

The energy loss processes that dominate the $\dot{p}$ term are Coulomb and ionization losses in the case of CR nuclei and synchrotron, inverse Compton, and bremsstrahlung losses in the case of CR leptons. For a detailed discussion on how these processes can be modeled, see Ref. [36]. Important ingredients for the modeling of these energy loss mechanisms are the gas density, the Galactic magnetic field, and the interstellar radiation field. As already mentioned, for the gas density, we follow the prescriptions of Ref. [32], while the magnetic field follows the model of Ref. [37], and the interstellar radiation field is the one described in Refs. [38,39].

The most important mechanism in our modeling of CR transport is spatial diffusion. CRs diffuse due to their resonant interaction with turbulent magnetic fields. This diffusion process is treated in terms of a diffusion coefficient $D_{xx}$, which, in the most general case, is a tensor of which the components are both spatially and rigidity dependent. Here, we will assume the simplest scenario in which diffusion is isotropic and homogeneous across the whole diffusive halo. Hence, we consider a scalar diffusion coefficient with no spatial dependence.

The rigidity dependence of the diffusion coefficient is set by the spectrum of the small-scale turbulence in the interstellar medium. In particular, a (one-dimensional) power-law spectrum $k^{-q}$ in wave number $k$ leads to a diffusion coefficient proportional to $\propto \mathcal{R}^{\delta}$, where $\delta = 2 - q$. We assume that the rigidity dependence of the diffusion coefficient is in the form of an $n$-times broken power law,

$$D_{xx}(\mathcal{R}) = D_0 \beta \left(\frac{\mathcal{R}}{\mathcal{R}_1}\right)^{\delta_1} \prod_{i=1}^{n} \left(1 + \left(\frac{\mathcal{R}}{\mathcal{R}_i}\right)^{1/s_i}\right)^{s_i(\delta_{i+1}-\delta_i)}, \quad (6)$$

where $D_0$ is a normalization factor, $\beta$ is the velocity of the particle under consideration, $\delta_i$ are the spectral indices in the rigidity regimes partitioned by the break rigidities $\mathcal{R}_i$, and the $s_i$ parametrize the smoothness of the rigidity breaks. For the Galactic diffusion coefficient, we assume two breaks, $n = 2$. In Fig. 1, we show the diffusion coefficient as a function of rigidity with the parameters as determined below.

Under a physical point of view, $\mathcal{R}_1$ (which we assume to be located at rigidities below 10 GV) is introduced following Ref. [40] to model in an effective way the damping of turbulence due to an (almost) isotropic distribution of cosmic rays. Moreover, as it will be detailed in the following, the presence of such a break is required to reproduce the behavior of the diffuse radio emission. On the other hand, the second break $\mathcal{R}_2$, which we expect to be at around 200 GV, is introduced as it provides a satisfactory fit to the most recent data from AMS [41,42], which have clearly shown that, at this rigidity, the fluxes of light secondary CRs (Li, Be, and B) exhibit identical hardening, stronger than the one that characterizes the flux of primary CRs (He, C, and O). A possible physical motivation for the existence of a break in the diffusion coefficient at around 200 GV could be a change in the origin of the turbulence that is responsible for CR diffusion. As an example, in Ref. [43], it has been suggested that such a break could be associated to the transition between diffusion in an external turbulence (as the one injected from SNRs) and diffusion onto CR self-generated waves (through the mechanism of streaming instability).

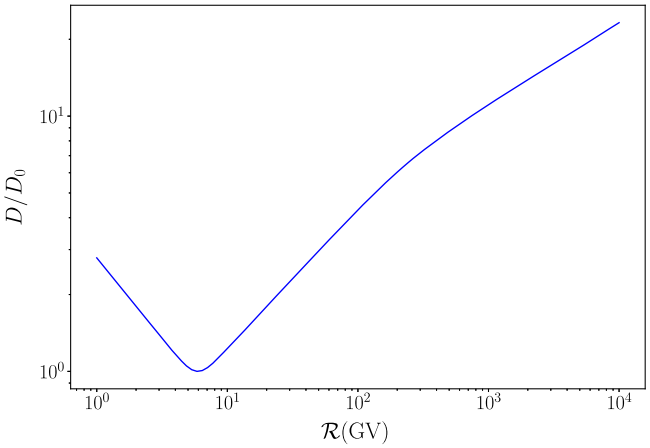


FIG. 1. Diffusion coefficient as a function of rigidity for the parameters determined below.

### C. Solar modulation

Before reaching Earth, CRs have to cross the heliosphere. This region hosts a turbulent magnetic field, together with a hot and ionized outflow called solar wind. The interaction of CRs with these agents impacts the CR distribution function, in a process known as solar modulation. Similarly to the case of Galactic propagation discussed above, also solar modulation can be modeled by means of a transport equation. Assuming a steady-state scenario and no injection of CRs in the heliosphere, this equation can be written as [44]

$$\vec{V} \cdot \nabla f - \nabla(K \nabla f) - \frac{\mathcal{R}}{3}(\nabla \cdot \vec{V}) \frac{\partial f}{\partial \mathcal{R}} = 0, \quad (7)$$

where $f$ is the CR phase space density (related to the number density by the relation $d\Psi = f(r,p) d^3 r d^3 p$), while $K$ is the spatial diffusion coefficient in the heliosphere and $\vec{V}$ is the velocity of the solar wind. Here, below, we discuss two ways of solving Eq. (7).

#### 1. Standard force-field approximation

A way of solving Eq. (7) is within the framework of the so-called force-field approximation introduced in Ref. [45]. Such a scenario is characterized by a series of simplifying assumptions. In particular, these assumptions consist in considering spherically symmetric boundary conditions at the heliospheric radius $R$, a radially directed and constant

solar wind velocity ($\vec{V} = V\hat{r}$), and a uniform and isotropic spatial diffusion (such that $K$ is a scalar). Moreover, one has to assume that the CR streaming (or radial current density), under the influence of diffusion and convection, is zero,

$$CVf - \kappa \frac{\partial f}{\partial r} = 0, \tag{8}$$

where $C = -(1/3)(\partial \ln f)/(\partial \ln p)$ is the Compton-Getting factor.

Under these assumptions, Eq. (7) simplifies to

$$\frac{\mathcal{R}V}{3K}\frac{\partial f}{\partial \mathcal{R}} + \frac{\partial f}{\partial r} = 0, \tag{9}$$

which can be solved with the method of characteristics. If one assumes $K = K_0\beta(\mathcal{R}/\mathcal{R}_1)$, in the relativistic case (where $\beta \approx 1$), the CR rigidity at the top of the Earth's atmosphere (i.e., after solar modulation) is given by

$$\mathcal{R}_{\rm TOA} = \mathcal{R}_{\rm LIS} - \phi, \tag{10}$$

where $\mathcal{R}_{\rm LIS}$ and $\mathcal{R}_{\rm TOA}$ are the local interstellar and Top-Of-Atmosphere rigidities, i.e., the rigidities before and after solar modulation, respectively, while

$$\phi = \frac{VR}{3K_0}\mathcal{R}_1 \tag{11}$$

is the force-field potential.[2] Once the relation between $\mathcal{R}_{\rm TOA}$ and $\mathcal{R}_{\rm LIS}$ is known, one can exploit the fact that the CR distribution function is conserved (as a consequence of Liouville's theorem) and write the CR top-of-atmosphere intensity as

$$J_{\rm TOA} = f\mathcal{R}^2_{\rm TOA} = \left(\frac{\mathcal{R}_{\rm TOA}}{\mathcal{R}_{\rm LIS}}\right)^2 J_{\rm LIS}. \tag{12}$$

### 2. Extended force-field approximation

To investigate the recent AMS time-dependent electron and positron data, we construct an extension of the force-field approximation, which is based on assuming a more general rigidity dependence of the CR diffusion coefficient in the heliosphere. In particular, we assume a broken power-law behavior:

$$K(\mathcal{R}) = K_0\beta\left(\frac{\mathcal{R}}{\mathcal{R}_b}\right)^{\gamma_1}\left(1 + \left(\frac{\mathcal{R}}{\mathcal{R}_b}\right)^{1/s}\right)^{s(\gamma_2-\gamma_1)}. \tag{13}$$

The physical motivation behind this assumption is that the rigidity dependence of the diffusion coefficient reflects the wave number dependence of the power spectrum of the turbulent component of the magnetic field. For resonant interactions between the CRs and the turbulent magnetic field, there is a one-to-one relation between the particle's rigidity and the turbulence's wave number, with the rigidity being inversely proportional to the resonant wave number. The range of wave numbers far above $2\pi/l_0$, where $l_0$ is the outer scale of turbulence, is referred to as the inertial range and is commonly modeled with a power spectrum $P(k) \propto k^{-q}$, e.g., with $q = 5/3$ for a Kolmogorov phenomenology. For smaller wave numbers, the turbulent power is usually significantly suppressed. Quasilinear theory then predicts resonant interactions for particles with rigidities small enough such that the resonant wave number is above $2\pi/l_0$ and a diffusion coefficient $K \propto \mathcal{R}^{2-q}$. For rigidities large enough such that the resonant wave number is below $2\pi/l_0$, interactions are nonresonant, and transport is in the small-angle scattering limit with $K \propto \mathcal{R}^2$. (See, for example, the recent discussion presented in Ref. [46].) Note that small-angle scattering is oftentimes considered for ultrahigh-energy cosmic rays for which the resonant scale would be beyond any conceivable outer scale of turbulence. However, the only scale in the problem is the outer scale of turbulence such that the problem can be easily scaled to environments with a smaller outer scale, like the heliosphere.

We assume $l_0$ to be equal to the coherence length of the heliospheric field, which has been estimated to be in a range that goes from 0.0079 [47] to 0.04 A.U. [48]. Such values roughly correspond to rigidities in the interval 3–12 GV. As it will be detailed in Sec. III, in our analysis, we will consider both $\gamma_1$ and $\gamma_2$ as free parameters. The reason is that, as discussed, for example, in Ref. [49], while the behavior of the spectral indices at scales much smaller and much larger than $l_0$ can be well understood in terms of the considerations illustrated above, the same cannot be said about the rigidity dependence of the diffusion tensor across the coherence length, the shape of which might depend on the turbulence model that is adopted and can even have a functional form that is more complicated than the broken power law that we are imposing here. The TOA rigidity is obtained as a function of LIS rigidity by integrating Eq. (9). Due to the complicated functional form of the diffusion coefficient, the relation between $\mathcal{R}_{\rm TOA}$ and $\mathcal{R}_{\rm LIS}$ is not as simple as in the original force-field model, cf. Eq. (10). However, the overall strength of modulation is still determined by the $\phi$-parameter as before; see Eq. (11).

AMS time-dependent electron and positron data cover a period of six years within the 24th solar cycle, from November 2011 (Bartels rotation number 2427) to April 2017 (Bartels rotation number 2506). In modeling the time dependence of the force-field potential, we consider the fact that this quantity should have two minima at the two extremes of the time interval that is covered by the dataset that we consider and a maximum that should correspond to the maximum of the solar activity in the solar cycle that we are considering (roughly April 2014). We parametrize $\phi(t)$ as the sum of a constant term, a Lorentzian function, and a hyperbolic tangent:

[2]It is important to point out that $\phi$ has the dimensions of a rigidity only in this specific case where $\beta = 1$ and $K \propto \mathcal{R}$.

$$\phi(t) = a + \frac{b - a - \frac{c-a}{2}}{1 + (\frac{t-t_0}{\tau})^2} + \frac{c-a}{2}\left(1 + \tanh\left(\frac{t-t_0}{\tau}\right)\right). \tag{14}$$

The time coordinate $t$ corresponds to the Bartels rotation number (which we shift to have the first data point at $t = 0$). The parameter $t_0$ identifies the position of the maximum, $\tau$ parametrizes the width of the maximum, $a = \phi(-\infty)$, $b \approx \phi(t_0)$, and $c = \phi(\infty)$.

## III. ANALYSIS

This section is devoted to the description of the different steps of our analysis. The analysis consists in fitting models of varying complexity to different combinations of datasets. Indeed, we start with a relatively small number of datasets, which can be reproduced by a relatively simple source spectrum. Adding in more datasets requires more complicated source spectra, and our analysis aims at understanding which particular dataset requires an additional feature in the source spectrum.

In particular, we start in Sec. III A by fitting to the AMS measurement of the boron-to-carbon ratio, which fixes the diffusion coefficient. Next, in Sec. III B, we determine the source spectrum of electrons and positrons by fitting to the radio spectrum at high latitudes and the high-energy data on the local electron and positron spectra as measured by AMS. In Sec. III C, we then add the low-energy Voyager I data for the all-electron spectrum beyond the heliopause, that is the presumed interstellar flux. Finally, in Sec. III D, we consider the recent AMS measurement of the time-dependent electron-positron data at energies of 1–50 GeV.

### A. Fitting to AMS B/C, proton and helium data

We fix the parameters $D_0, \delta_1, \delta_2, \delta_3, \mathcal{R}_1$, and $\mathcal{R}_2$ of Eq. (6) by fitting the AMS data on the boron-to-carbon ratio (B/C) [41]. In addition, we fit also the AMS data on the CR proton [4] and helium [42], since the spectra of these CR particle species are needed to compute the secondary $e^{\pm}$ emission, as discussed in Sec. II A. The systematic uncertainties of the different data points are treated as detailed in Appendix A.

The proton and helium injected spectra are assumed to be broken power laws in rigidity. This means that for both species the function $g(\mathcal{R})$ that appears in Eq. (1) is assumed to be of the form

$$g(\mathcal{R}) = \begin{cases} \left(\dfrac{\mathcal{R}}{\mathcal{R}^*}\right)^{-\theta_1} & \text{for } \mathcal{R} \le \mathcal{R}^*, \\ \left(\dfrac{\mathcal{R}}{\mathcal{R}^*}\right)^{-\theta_2} & \text{for } \mathcal{R} > \mathcal{R}^*, \end{cases} \tag{15}$$

where $\mathcal{R}^*$ is the position of the rigidity break, where the spectral index passes from $\theta_1$ to $\theta_2$. For all CR species heavier than helium, we adopt the helium spectral indices.

TABLE I. Best-fit parameters for the fit to B/C, proton, and helium data. The free normalizations of the proton and helium injection spectra [expressed by the parameter $Q_0$ in Eq. (1)] is parametrized in terms of the values of the final fluxes $\Phi_p$ and $\Phi_{\rm He}$ at the reference rigidity $\mathcal{R}_{\rm ref} = 30$ GV.

| | | | | | | | $\Phi_p(\mathcal{R}_{\rm ref})$ | | | | $\Phi_{\rm He}(\mathcal{R}_{\rm ref})$ | | | | | |
|---|---|---|---|---|---|---|---|---|---|---|---|---|---|---|---|---|
| $D_0$ $10^{28}$ cm$^2$ s$^{-1}$ | $\delta_1$ | $\delta_2$ | $\delta_3$ | $\mathcal{R}_1$ (GV) | $\mathcal{R}_2$ (GV) | $s_1$ | $s_2$ | ((GeV m$^2$ s sr)$^{-1}$) | $\theta_{p,1}$ | $\theta_{p,2}$ | $\mathcal{R}_p^*$ (GV) | (((GeV/n)m$^2$ s sr)$^{-1}$) | $\theta_{\rm He,1}$ | $\theta_{\rm He,2}$ | $\mathcal{R}_{\rm He}^*$ (GV) | $\phi_{\rm B/C}$ (GV) | $\phi_{\rm He}$ (GV) | $\phi_p$ (GV) |
| 3.76 | −0.63 | 0.55 | 0.32 | 5.86 | 240.68 | 0.11 | 0.46 | 1.21 | 2.89 | 2.38 | 5.92 | 0.53 | 2.63 | 2.29 | 7.52 | 0.72 | 0.60 | 0.65 |

TABLE II. $\chi^2$ values associated to the different datasets.

| $\chi^2_{\mathrm{B/C}}$/d.o.f. | $\chi^2_{\mathrm{He}}$/d.o.f. | $\chi^2_{\mathrm{p}}$/d.o.f. |
|---|---|---|
| 25.61/58 | 61.44/59 | 45.80/55 |

It is important to point out that, because of this, the fits to B/C and to He data are not independent of each other.

The proton, helium, and B/C data that are considered here in the fit are *solar modulated* data. As we are mainly concerned with CR electrons and positrons, we treat solar modulation in terms of the standard force-field model described in Sec. II C 1. In our fit, we allow for different values of the Fisk potential for the different observables under consideration.

Another remark that has to be made is that when determining the position of the low-rigidity break in the diffusion coefficient $\mathcal{R}_1$ we consider the value of this parameter that provides the best fit to the diffuse synchrotron emission. More in detail, we follow an iterative procedure where we perform several fits of proton, helium, and B/C data under different flat priors for the $\mathcal{R}_1$ parameter. Among the configurations of the parameters that are obtained in this way, we isolate the ones that provide an acceptably good fit to nuclear data (i.e., we exclude the ones for which $\chi^2/\mathrm{d.o.f} > 1$), and we select the best-fit configuration as the one that is in best agreement with radio data, fitted within the *0 breaks model* (both the model and the fit will be discussed in the next section). It is worth stressing that, as mentioned above, radio observations require a break in the diffusion coefficient; indeed, when fitting the 0 breaks model to radio data without the low-energy break in the diffusion coefficient, the $\chi^2$ we obtain is 19.5 (for six data points).

The best-fit parameters found in the fit are reported in Table I, while the $\chi^2$ values associated to the different datasets can be found in Table II, and the best-fit configurations are shown together with AMS B/C and proton data in Fig. 2. The quality of the fit is remarkably good, as it can be seen, in the case of the proton and B/C data, from the pulls that are shown in the lower panel of the plots. One potential issue could be represented by the fact that the rigidity breaks in the proton and helium source terms are found to be very close to the low-rigidity break in the diffusion coefficient. Similar results were already found in Ref. [25] for purely diffusive CR transport models very similar to the one we are discussing here. Given the lack of theoretical arguments that can be invoked to motivate the existence or the location of such breaks in the H and He source terms, it is difficult to establish if their vicinity to the break in the diffusion coefficient represents an issue or not. Moreover, it is to be expected that the rigidities at which all the breaks are found (both in the diffusion coefficient and in the source terms) would shift depending on the treatment of solar modulation. In any case, even if a thorough investigation on this issue is beyond the scope of this paper, it is clear that the vicinity of the breaks introduces a correlation between the parameters $\delta_1$, $\theta_{p,1}$, and $\theta_{He,1}$.

### B. Fitting to radio and AMS local high-energy electron and positron data

CR electrons and positrons can be injected in the ISM through a variety of processes as discussed in Sec. II A. Here, we assume the source term of primary electrons injected by SNRs to be a simple power law; i.e., the rigidity dependence of Eq. (1) is given by

$$g(\mathcal{R}) = N_{e^-}\left(\frac{\mathcal{R}}{\mathcal{R}_0}\right)^{-\alpha_2}. \tag{16}$$

As discussed in Sec. II A, high-energy positrons and electrons are assumed to be accelerated by an extra source, with a rigidity spectrum that depends on two parameters: the normalization $N_{\mathrm{x}}$ and the spectral index $\Gamma_{\mathrm{x}}$. Concerning the secondary component produced by spallation

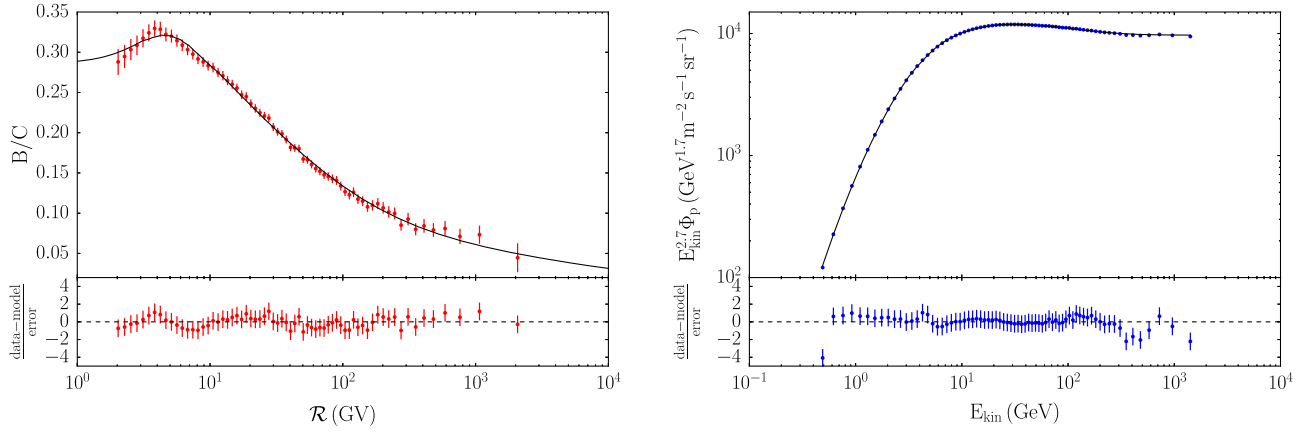


FIG. 2. The left and right panels show, respectively, the boron-to-carbon ratio and the proton flux for the best-fit configuration of our model, in comparison with AMS data. B/C and proton data are taken, respectively, from Refs. [41] and [4]. For both plots, the lower panels show the pulls.

TABLE III. Best-fit parameters for the three fits to different combinations of datasets considered in our analysis. The parameters $\Phi_{e^-}$ and $\Phi_x$ correspond to the fluxes associated to SNRs and to the extra component at $\mathcal{R} = 30$ GV, the normalizations of which are a function of the free parameters $N_{e^-}$ and $N_x$, respectively. The uncertainty on each parameter is determined through the procedure described in Appendix A.

| Model | $\Phi_{e^-}$ $(\mathrm{GeV}^{-1}\mathrm{m}^{-2}\mathrm{sr}^{-1}\mathrm{s}^{-1})$ | $\Phi_x$ $(\mathrm{GeV}^{-1}\mathrm{m}^{-2}\mathrm{sr}^{-1}\mathrm{s}^{-1})$ | $\Gamma_x$ | $\mathcal{R}_a$ (GV) | $\mathcal{R}_b$ (GV) | $\alpha_1$ | $\alpha_2$ | $\alpha_3$ | $f_B$ |
|---|---|---|---|---|---|---|---|---|---|
| 0 breaks | $(4.21 \pm 0.05) \times 10^{-3}$ | $(2.38 \pm 0.02) \times 10^{-4}$ | $1.60 \pm 0.01$ | ⋯ | ⋯ | ⋯ | $2.58 \pm 0.01$ | ⋯ | $3.08^{+0.02}_{-0.05}$ |
| 1 break | $(4.21 \pm 0.05) \times 10^{-3}$ | $(2.37 \pm 0.01) \times 10^{-4}$ | $1.60^{+0.01}_{-0.03}$ | $0.109^{+0.005}_{-0.003}$ | ⋯ | $2.13^{+0.01}_{-0.02}$ | $2.57 \pm 0.02$ | ⋯ | $3.07^{+0.03}_{-0.08}$ |
| 2 breaks | $4.37^{+0.01}_{-0.06} \times 10^{-3}$ | $2.39^{+0.06}_{-0.02} \times 10^{-4}$ | $1.63 \pm 0.01$ | $0.411^{+0.001}_{-0.004}$ | $83.4^{+1.8}_{-0.1}$ | $2.12^{+0.002}_{-0.012}$ | $2.69 \pm 0.01$ | $2.53 \pm 0.01$ | $2.48^{+0.04}_{-0.01}$ |

processes, it is modeled as in Eq. (3), with the proton and helium spectra determined through the fitting procedure described in the previous paragraph.

With all this considered, the model that we are investigating here, which we label the 0 breaks model, is characterized by five free parameters. Four of these parameters are directly associated to the electrons and positrons source terms. They are the spectral index $\alpha_2$ and the normalization $N_{e^-}$ of the electron spectrum injected by SNRs [see Eq. (16)] and the spectral index $\Gamma_x$ of the $e^{\pm}$ spectrum injected by the extra component and its normalisation $N_x$ [see Eq. (2)]. In addition, the synchrotron flux depends on the strength of the magnetic field $B(\vec{r})$ which varies as a function of position. We adopt a model, with a simple exponential dependence, on the galactocentric radius $r$ and the distance from the disk, $z$,

$$B(r, z) = B_0 \exp[-(r - r_0)/\rho - |z|/z_0]. \quad (17)$$

Our results are rather insensitive to the specific values of $r_0$, $\rho$, and $z_0$, and so we adopt $r_0 = 8.5$ kpc, $\rho = 8$ kpc, and $z_0 = 2$ kpc. However, we allow for the normalization to float in the fit by a factor $f_B$ with respect to the fiducial value of $B_0 = 3$ $\mu$G. We expect for $f_B$ to differ from 1 by a factor of a few at most. It is important to remark that $f_B$ is expected to be degenerate with respect to the halo size $H$. More specifically, one has $f_B^2 \propto H^{-1}$ as a consequence of the fact that the synchrotron signal is sensitive to the total magnetic energy of the Galaxy.[3]

We determine the five free parameters by fitting to radio and AMS local high-energy electron and positron data [20,51]. In building the dataset of radio measurements to be used in the fit, we follow the approach described in Refs. [50,52–55], which consists of considering those radio surveys that display a complete (or nearly complete) sky coverage at several frequencies in the megahertz to gigahertz interval (more precisely, 22 MHz, 45 MHz, 408 MHz, 1420 MHz, 2326 MHz, 23 GHz, 33 GHz, 41 GHz, 61 GHz, and 94 GHz). For each one of these frequencies, an average flux is estimated by integrating the sky maps produced by the respective survey over the high-latitude region, once the contribution from the Galactic plane and from radio sources is removed through the application of the WMAP extended temperature analysis mask [56]. The uncertainty associated to the radio flux in each frequency bin is the result of the variance of the flux in the region of the sky under consideration. It is important to point out that in our analysis of the synchrotron data not all the frequencies enter in the calculation of the $\chi^2$. In particular, we will not include in our assessment of the goodness of the fit the frequencies above 10 GHz as at these frequencies the radio emission is expected to receive important contributions from free-free and thermal dust emission. Therefore, one can consider the radio flux determined at these frequencies as an upper limit to the diffuse emission from CR electrons and positrons.

When fitting to AMS high-energy data, we adopt the prescription described in Appendix A to treat systematic uncertainties and to determine an uncertainty on the best-fit parameters. Furthermore, we consider only measurements above a minimum energy, which we set at $E_{\mathrm{cut}} = 40$ GeV. The reason for this choice is that we compare AMS data to the unmodulated LIS. This means that we have to consider energies that are sufficiently large that the effect of solar modulation can be considered negligible with respect to the accuracy of the data. We have checked that alternative choices of $E_{\mathrm{cut}}$ do not change our results in a significant way. More details on the impact that solar modulation has on the flux at different energies will be provided in Sec. III D when we will describe the fit to the AMS time-dependent data.

Within the scenario that we have described in the previous section, characterized by a double break in the rigidity dependence of the spatial diffusion coefficient, this simple model is able to fit remarkably well all the datasets we are considering. Our best-fit parameters are reported in the first row of Table III, while the values of the $\chi^2$ associated to each dataset are reported in the first row of Table IV. The best-fit configuration is shown in comparison with data in the upper line and lower left panels of Fig. 3 (specifically, the 0 breaks model is represented by the magenta dotted-dashed lines). One important point to

[3]Moreover, as discussed in Ref. [50], one can use the latitude profile of the synchrotron emission at 408 MHz that allows one to place a lower bound on the halo size at 2 kpc.

TABLE IV. $\chi^2$ values associated to the fit of the different models to the datasets considered in our analysis.

| Model | $\chi^2_{e^-}$ HE/d.o.f. | $\chi^2_{e^+}$ HE/d.o.f. | $\chi^2_{\rm radio}$/d.o.f. | $\chi^2_{\rm Voy}$/d.o.f. | $\chi^2_{e^-}$ TD/d.o.f. | $\chi^2_{e^+}$ TD/d.o.f. | $\chi^2_{e^+/e^-}$ TD/d.o.f. |
|---|---|---|---|---|---|---|---|
| 0 breaks | 27.5/20 | 23.0/23 | 3.3/4 | … | … | … | … |
| 1 break | 28.0/20 | 23.0/23 | 3.2/4 | 12.1/6 | … | … | … |
| 2 breaks | 17.9/18 | 26.3/23 | 6.5/4 | 12.9/6 | 21654/3808 | 6533/3812 | 4510/3798 |

remark is that the fit requires the slope of the primary electron spectrum to be rather hard, and this has a great impact at low energies, where, as can be seen in the top left panel of Fig. 3, the electron LIS can even be *below* the data (in particular in the region below 40 GeV, not included in the fit). This will pose issues when the low-energy data (and solar modulation) will be taken into account, as we will discuss in detail later.

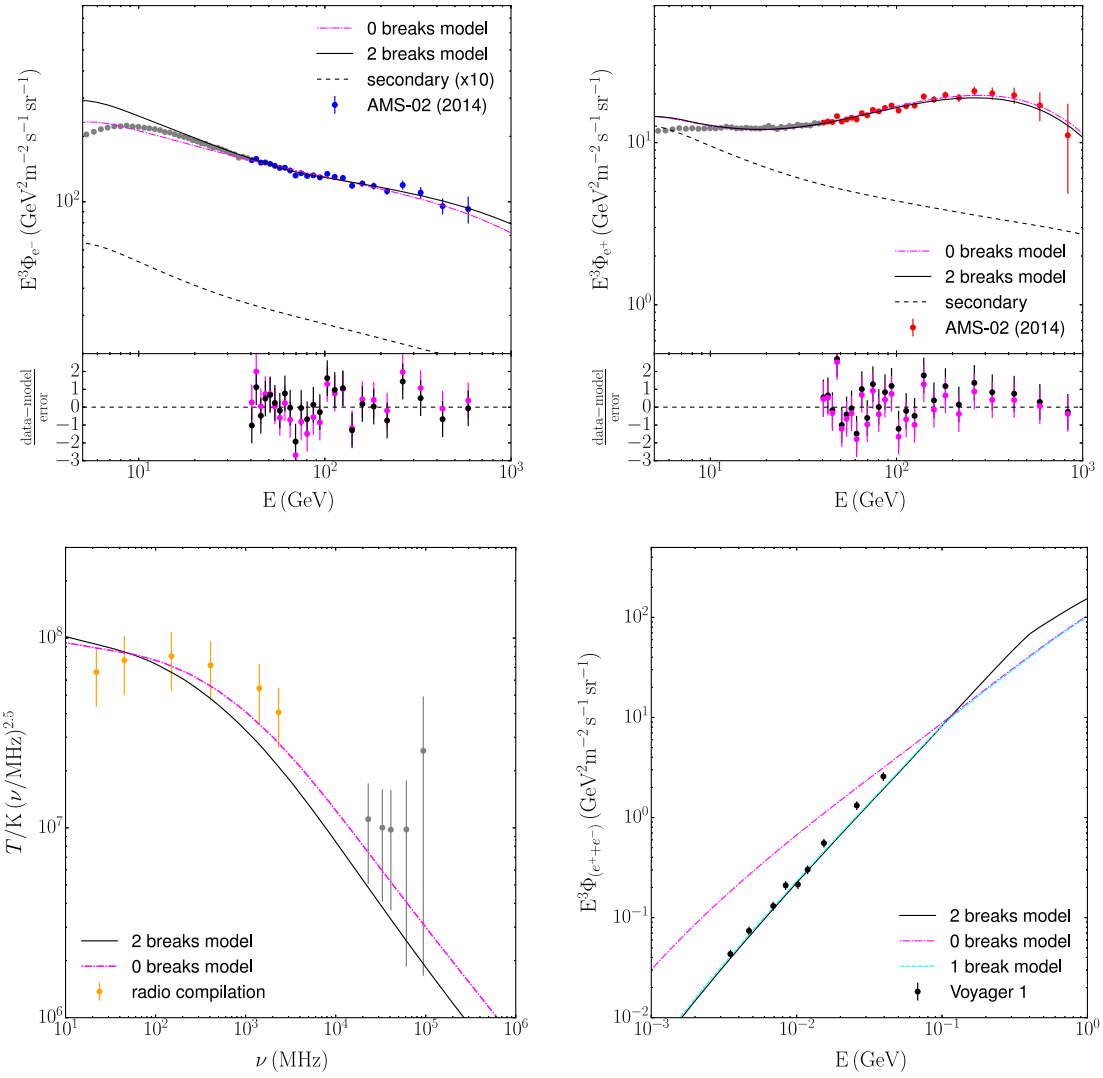


FIG. 3. In the top row, the electron (left panel) and positron (right panel) LIS predicted by the 0 breaks (magenta dot-dashed lines) and 2 breaks (black solid lines) models described in the text are shown together with AMS data [20,51]. We also show the secondary component only (dashed black lines), which is the same in both models. In each plot, gray data points are the ones that have been excluded in the fitting procedure. The panels below each plot show the pulls (data-model/ $\sigma_{\rm exp}$). In both plots, the LIS predicted by the 1 break model is not shown, as it is undistinguishable from the one of the 0 breaks model. The bottom left panel illustrates the behavior of the predicted synchrotron emission, for both the 0 breaks and the 2 breaks models in comparison with data. Data points that are not used in the fit are in gray. In the bottom right panel, the all-electron flux predicted at low energies by the two models and by the 1 break model is shown together with data from Voyager 1 [25].

### C. Fitting to radio, high-energy, and Voyager data

Our intent in this part of the analysis is to constrain the very low-energy range (i.e., below 100 MeV) of the electron LIS. To this end, we consider the measurements of the total electron flux made by Voyager 1 [25] at energies between 2.7 and 74.1 MeV.

As seen in the bottom right panel of Fig. 3, the model, which was found in the previous part of the analysis to provide a remarkably good fit to high-energy and radio data, produces a total electron LIS that is in disagreement with Voyager data. More precisely, the spectrum appears to be too soft, and its normalization seems too large. If the parameters of the 0 breaks model are refitted including Voyager data, one gets chi-square values of 69 and 140 with respect to Voyager and AMS high-energy electron data, respectively. We are thus led to adopt a break also in the source spectrum of primary electrons,

$$g(\mathcal{R}) = \begin{cases} \left(\frac{\mathcal{R}}{\mathcal{R}_0}\right)^{-\alpha_1} & \text{for } \mathcal{R} \leq \mathcal{R}_a, \\ \left(\frac{\mathcal{R}_a}{\mathcal{R}_0}\right)^{-\alpha_1} \left(\frac{\mathcal{R}}{\mathcal{R}_a}\right)^{-\alpha_2} & \text{for } \mathcal{R} > \mathcal{R}_a. \end{cases} \tag{18}$$

The model that we are considering here, which we label the *1 break model*, consists of seven free parameters, which are the five that characterized the 0 breaks model, plus $\mathcal{R}_a$ and $\alpha_1$. The best-fit parameters and the $\chi^2$ associated to each dataset are reported, respectively, in Tables III and IV, and the low-energy total electron LIS is shown, together with Voyager data in the bottom right panel of Fig. 3 (specifically, the 1 break model is represented by the dashed cyan line). The goodness of fit with respect to this dataset has significantly improved.

### D. Fitting to radio, high-energy, Voyager and AMS time-dependent data

In the previous sections, we have investigated the electron and positron LIS. We now turn our attention to the investigation of the *solar modulated* fluxes. The idea is that modulated fluxes can provide additional constraints to our models of the LIS. As discussed above, for example, the fit to radio data requires a rather hard electron spectrum which at energies $\mathcal{O}$ (1–10) GeV might cause the LIS to even be lower than the measured spectrum, thus leaving very little room, or even no room at all, for solar modulation. A fit including low-energy local measurements is mandatory in order to assess this potential issue.

We use the local electron and positron fluxes measured by the AMS experiment in the 1–50 GeV energy range. We model solar modulation as described in Sec. II C 2. We tune our model, which we label *2 breaks model*, by performing a global fit to all the datasets considered in the previous steps of the analysis (radio, high-energy, and Voyager data) together with the time-dependent electron and positron data from AMS. In fitting the high-energy electron and positron spectra, we consider only data above 50 GeV, thus avoiding any overlap with the time-dependent datasets. In building the model, we start from the one described in the previous section (i.e., with a low-energy break in the electron spectrum in order to reproduce Voyager data), and then we add the possibility of having a second break in the electron spectrum at high energies (here, "high energies" means outside the regime where solar modulation has an impact). This addition of a second break is motivated by our expectation that a model able to correctly reproduce solar modulated data will be characterized by an electron spectrum at $\mathcal{O}(1-10)$ GeV energies, which will probably be softer than the one found in the previous steps of the analysis. If the spectrum is softer at low energies, a spectral hardening will be required to reproduce the high-energy end of the electron spectrum measured by AMS. Adding a break adds two free parameters to the model, which now consists of nine parameters associated to the modeling of the positron and electron LIS, in addition to the parameters associated to the solar modulation model.

The results of the fit are reported in the bottom row of Table III, while the various observables related to the positron and electron LIS are shown in Fig. 3, and the $\chi^2$ values associated to the different datasets are listed in Table IV. In addition, the electron and positron LIS are reported in tabulated form in Appendix B. The LIS are substantially modified now that solar modulated data are taken into account. In particular, the electron LIS is significantly softer at intermediate energies ($\Gamma_2$ changes from 2.57 to 2.69). This requires a relatively strong hardening in order to fit high-energy electron data. Overall, the fit to high-energy electron data is significantly better than in the previous cases we considered. Moreover, as predicted, the fit to radio data worsens as a result of the electron LIS being steeper at low energies, but it is still in acceptably good agreement with data. Another important consequence of the necessity to have a softer electron spectrum at $\mathcal{O}(1-10)$ GeV energies is that the low-energy spectral break needed to fit Voyager data gets shifted to larger energies (it moves from 109 to 411 MeV). This is illustrated in the bottom right panel of Fig. 3.

The results of the fit to the time-dependent AMS electron and positron fluxes are shown in Figs. 4 and 5, while the best-fit solar modulation parameters are reported in Table V. Our model provides a satisfactory fit to the long-term behavior of both the positron and electron spectra, across the whole energy range covered by AMS time-dependent data. However, it is also manifest that there are several short-term variations in both spectra that cannot be described within the framework of our model. Indeed, as discussed in Sec. II C 2, our solar modulation model is

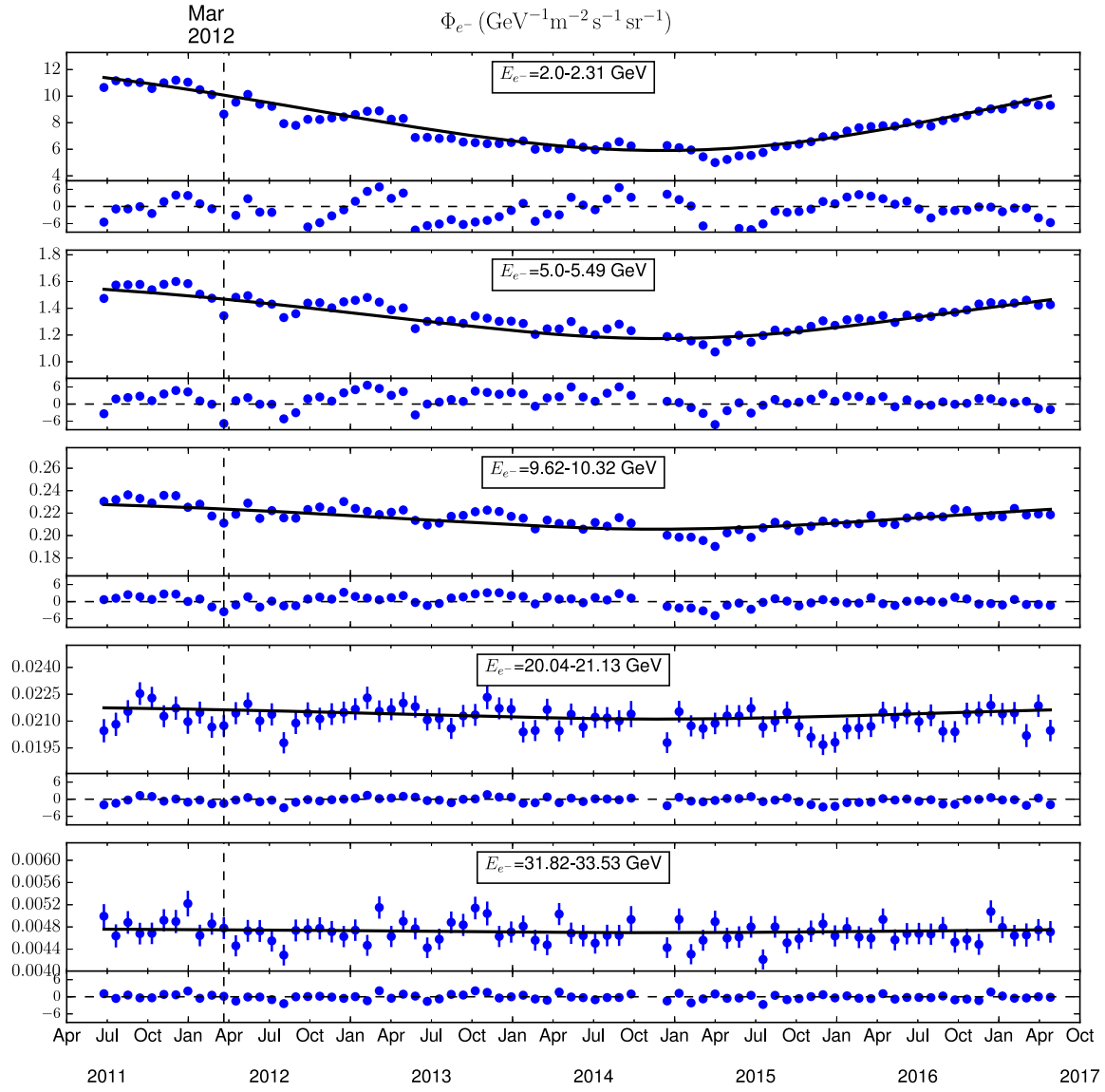


FIG. 4. Electron time-dependent fluxes, as predicted by our model (solid lines) and as measured by AMS [24] (points). Each panel refers to a specific energy (as reported in the labels).

based on the assumption that the force-field potential varies smoothly with time, which is not the case for the short-term events that appear here. This complex structure of short-term fluctuations is the result of different solar phenomena, namely, coronal mass ejections and solar wind streams, which can determine both increases (solar energetic particle events) and decreases (Forbush decrease) of the fluxes of CRs that reach Earth. These variations are typically much larger than the experimental uncertainty associated to the AMS measurement of the fluxes, in particular at the lowest energies. This is illustrated in Figs. 4 and 5 for the case of the March 2012 Forbush decrease, which is one of the strongest solar events recorded during the AMS data-taking period [57]. The fact that the fluctuations in the spectra associated to short term events are larger than the experimental uncertainties on the data points is particularly true for the electron spectrum, which is characterized by the smallest uncertainty, and this explains the large $\chi^2$ value associated to this dataset. Figure 6 illustrates the predicted $e^+/e^-$ ratio, and it can be seen that short-term events have a much more limited impact on the $e^+/e^-$ ratio.

It is important to stress that the introduction of the second break in the SNR source term is necessary in order to get a good fit to the time-dependent data. Indeed, when fitting the parameters of the 1 break model to all the datasets that we consider here, we get a fit to the electron time-dependent data which is characterized by a chi-square per degree of freedom of 6.7. This value might seem not much higher than the one we get for the 2 breaks model

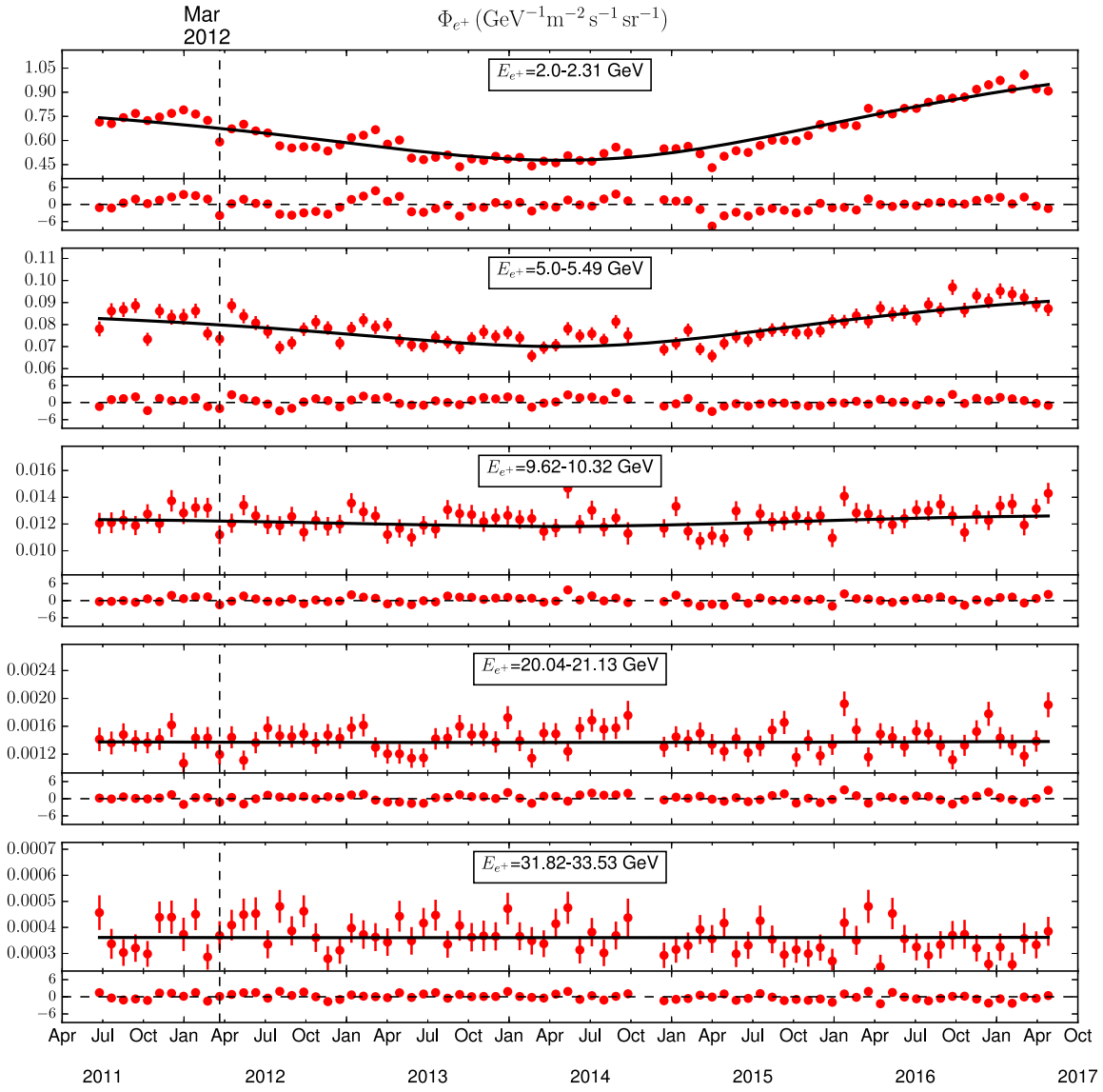


FIG. 5. Positron time-dependent fluxes, as predicted by our model (solid lines) and as measured by AMS [24] (points). Each panel refers to a specific energy (as reported in the labels).

(5.7), but if one looks at the quality of the fit in the single energy bins, one finds that at energies around 10 GeV the 2 breaks model performs much better; as an example, in the [9.62, 10.32] GeV energy bin, the chi-square per degree of freedom is 2.7 for the 2 breaks model and 5.5 for the 1 break model. This occurs because, as discussed above, the LIS that is found without a high-rigidity break in the SNR source term falls below data, and this leaves no room for solar modulation.

In order to better assess the performance of our solar modulation model in fitting the average trend of the spectra, we compare in the left panel of Fig. 7 the maximum fluctuation of the electron spectrum that our fit predicts with the one that is actually observed in AMS data and with

TABLE V. Best-fit parameters for the solar modulation parameters [see Eqs. (13) and (14)].

| Particle | $\gamma_1$ | $\gamma_2$ | $\mathcal{R}_b$ (GV) | $a$ (GV) | $b$ (GV) | $c$ (GV) | $t_0$ (Bartels rotation) | $\tau$ (Bartels rotation) |
|---|---|---|---|---|---|---|---|---|
| Electron | $1.32^{+0.05}_{-0.03}$ | $1.76^{+0.10}_{-0.01}$ | $5.71^{+0.26}_{-0.35}$ | $0.12^{+0.02}_{-0.03}$ | $0.585^{+0.016}_{-0.011}$ | $0.067^{+0.027}_{-0.035}$ | $2474.54 \pm 0.01$ | $34.01^{+0.74}_{-1.47}$ |
| Positron | $1.25^{+0.01}_{-0.05}$ | $2.29^{+0.29}_{-0.33}$ | $5.13^{+0.52}_{-0.93}$ | $0.12^{+0.01}_{-0.04}$ | $0.413^{+0.031}_{-0.011}$ | $0.010^{+0.002}_{-0.03}$ | $2467.5 \pm 0.7$ | $26.12^{+3.01}_{-0.83}$ |

the fluctuation that results from a direct fit of the spectrum with a harmonic function of period $T$,

$$\Phi_{e^-}(t) = A + B\cos\left(\frac{2\pi(t-t_0)}{T}\right), \tag{19}$$

where the parameters $A$, $B$, and $T$ are taken as free for each one of the energy bins of AMS data. In particular, the period $T$ is typically found to be around 8 years. The variation predicted by our model is in good agreement with the one resulting from the harmonic fit, which, albeit not a physically motivated model, certainly offers a good assessment of the maximum fluctuations that can be found within the framework of a model where the solar modulation parameters are assumed to have a smooth dependence on time. The behavior of the harmonic fit at high energies is that such a fit is noise dominated because of the increased uncertainty associated with AMS data. By comparing the fluctuations observed in the data with the ones predicted by the harmonic fit and by our model, one can estimate the impact of short-term solar events. The results shown in the left panel of Fig. 7 allow also for an estimate of the maximum impact of solar modulation on the electron flux; if one considers only the long-term fluctuations, such impact is still above 1% at 20 GeV, while if one takes into account also short-term events, the impact reaches 4%.

In the right panel of Fig. 7, we show the unmodulated momenta $p_{\rm IS}$ as a function of time for modulated momenta $p_{\rm TOA} = 0.1, 2$ and $10\ {\rm GeV}/c$, based, respectively, on

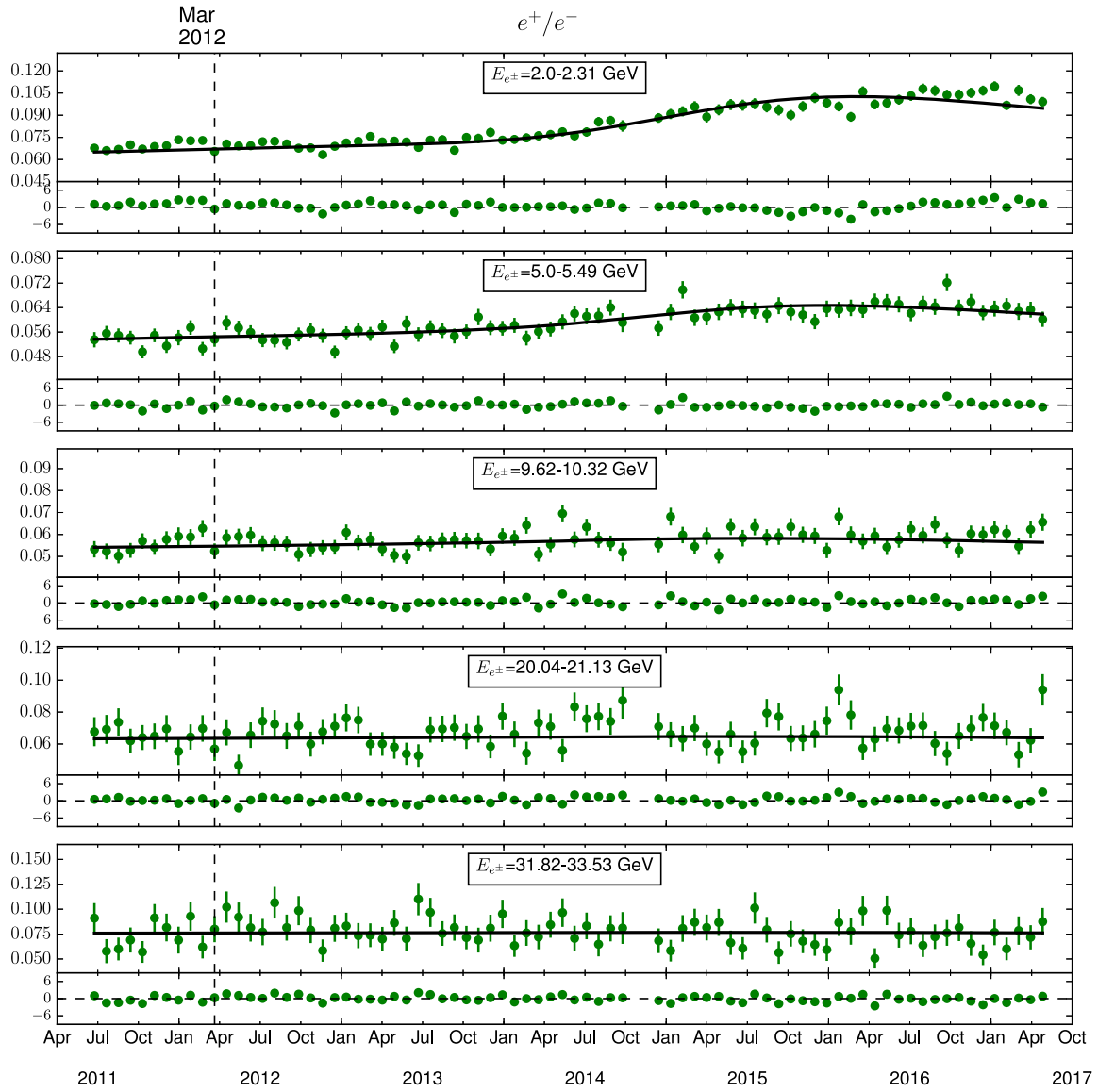


FIG. 6. Positron-to-electron time-dependent ratio, as predicted by our model (solid lines) and as measured by AMS [24](points). Each panel refers to a specific energy (as reported in the labels).

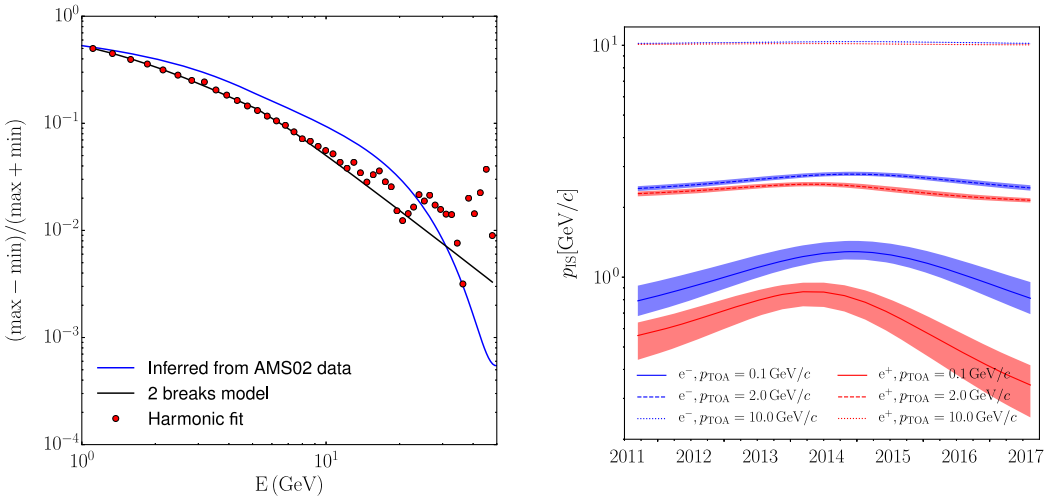


FIG. 7. Left: Maximum fluctuation of the electron spectrum as a function of energy, as inferred from AMS data (blue curve) and as predicted within the framework of our solar modulation model (solid black line) or by means of the fit with the harmonic function of Eq. (19) (red points). Right: Unmodulated momentum $p_{IS}$ as a function of time for modulated momenta $p_{TOA} = 0.1, 2$, and 10 GeV/$c$. The shaded bans reflect the error on the fitted solar modulation parameters, cf. Table V. Note that, while the modulation to momenta $p_{TOA} > 1$ GeV/$c$ is constrained by AMS data, the modulation at lower momenta is an extrapolation.

Eqs. (14) and (13) with the parameters of Table V. First, there is the usual overall trend with energy, in that high-energy electrons and positrons are less affected by solar modulation than low-energy electrons and positrons. (Compare, for instance, the $p_{TOA} = 0.1$ GeV/$c$ curves with the $p_{TOA} = 10$ GeV/$c$ ones.) Second, modulation is markedly charge-sign dependent; electrons are modulated more strongly than positrons, in particular from approximately 2014 onward, whereas at earlier times both are modulated in similar ways. This is compatible with our expectations as most of the AMS time-dependent data collected in Ref. [24] refer to a period of positive polarity of the heliospheric magnetic field. Indeed, as discussed in Ref. [58], because of drifts, positively charged particles at Earth have propagated across polar directions, while the negatively charged particles have traveled along the heliospheric current sheet (HCS). Due to the waviness of the HCS, negatively charged particles travel longer distances and are thus subject to stronger adiabatic losses. Our solar modulation model does not explicitly feature drift effects, but we allow for different $\phi$ functions for electrons and positrons, and thus the modulation can be different if the data require it. At earlier times, that is between approximately 2011 and 2014, solar activity was

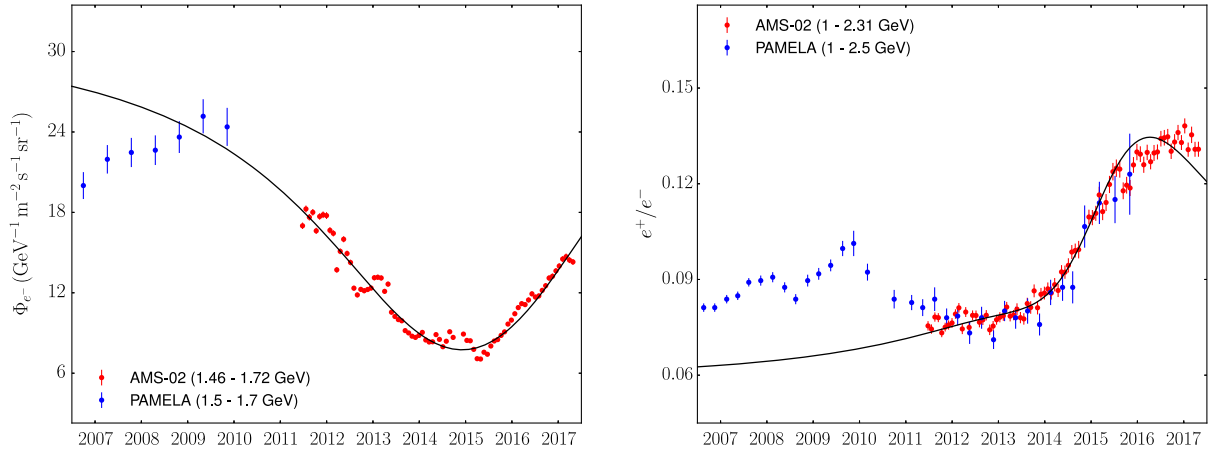


FIG. 8. Electron flux (*left panel*) and electron-to-positron ratio (*right panel*) in two different energy bins, as predicted from our model with the parameters of Table V compared with AMS data [24] (red points) and PAMELA data [23,59] (blue points). In the case of the ratio, the AMS data points have been integrated over several energy bins, in order to have the maximal compatibility with the PAMELA energy bins.

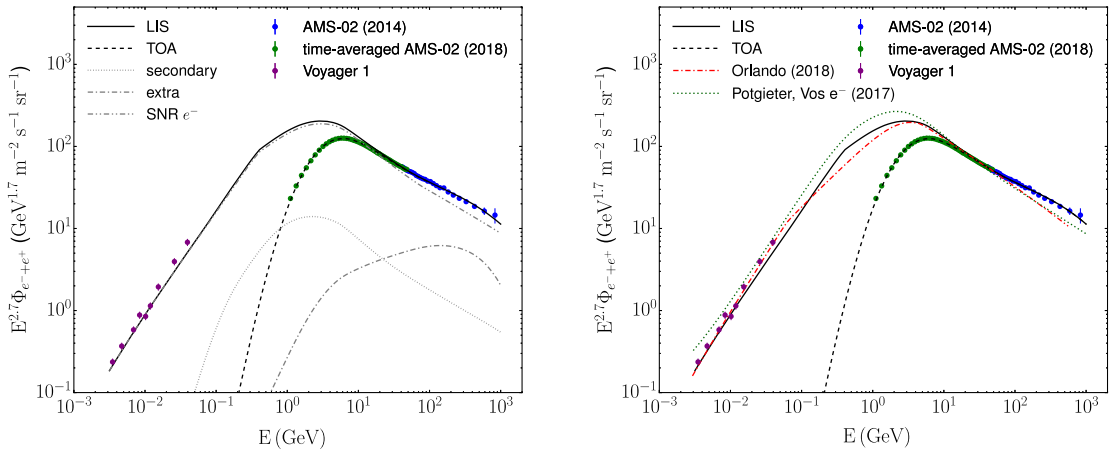


FIG. 9. Left: All electron spectrum, plotted together with the different datasets considered in this work. The green points represent the average over the AMS data-taking period of the time-dependent datasets of Ref. [24], while the dashed black line is the average over the same time period of the all-electron flux predicted by our solar modulation model with the best-fit parameters of Table V. The gray lines show the contributions from the different electron and positron sources. Right: Same as in the left panel, with the addition of the $e^+ + e^-$ LIS of Ref. [55] (red, dot-dashed line) and the $e^-$ LIS from Ref. [60] (green, dotted line).

at a maximum, and electrons and positrons will have been modulated similarly. This is in line with the curves in the right panel of Fig. 7 being closer together.

Despite the fact that our solar modulation model is able to reproduce the average spectra remarkably well, and with parameters that are compatible with our expectations, a word of caution is in order about the possibility of using the parameters of our model to make predictions outside of the AMS data-taking period. Indeed, since our model is based on a simplified description of solar modulation and, at present, AMS data cover only a limited fraction of the solar cycle, we do not expect our model to have strong predictive power. To better illustrate this point, we plot in Fig. 8 the prediction of our model, extended in the past by assuming a 22 years periodicity for the electron and positron force-field potentials, compared to the $e^-$ flux and the $e^+/e^-$ ratio measured by PAMELA [23,59]. The predictivity of our solar modulation model will certainly improve if its parameters were tuned on a dataset extended over a whole solar cycle, but still it has to be taken into account that different solar cycles might also be very different, and therefore a simple periodicity of the force-field potentials might not be a realistic assumption.

## IV. SUMMARY AND OUTLOOK

We have presented a model of the cosmic-ray electron and positrons fluxes over a wide range of energies, from the mega-electron-volt to the tera-electron-volt domain, reproducing not only fluxes measured locally, but also the Galactic radio background and measurements outside the heliosphere. For sources of electrons and positrons we have considered SNRs, charge-symmetric extra sources, and spallation processes in the interstellar medium. Moreover, we have assumed the Galactic transport of electrons and positrons to be purely diffusive. In order to motivate the spectral breaks needed in the spectrum of SNRs, we have carefully considered the influence of different datasets. A satisfactory fit to the high-energy domain of the electron and positron fluxes measured by AMS and to the diffuse radio emission can be achieved with a simple power law for the electrons injected by SNRs. However, such a model overproduces electrons at $\mathcal{O}(\mathrm{MeV})$ energies as measured by Voyager I. Instead, a spectral break in the SNR spectrum is required. Including in our fit also recent time-dependent electron and positron top-of-atmosphere fluxes requires modeling the effects of solar modulation, which we have performed within a simple extension of the standard force-field approximation. We have shown that the fit to solar modulated data requires the electron spectrum injected by SNRs to be steeper at $\mathcal{O}(1-10)$ GeV energies, and this makes a second spectral break at high energies necessary to fit the electron flux. In addition, the fit to the AMS time-dependent datasets has also proven that our solar modulation model works very well in reproducing the long-term trends of the low-energy electron and positron fluxes.

We stress here that in this work we have worked under the hypothesis that CR transport in the Galaxy is purely diffusive and this clearly has an impact on the results that we have found. In particular, one should expect that if other processes (e.g., reacceleration and convection) are taken into account the observed data could be fitted by different electron and positron LIS, namely with a different configuration of the spectral breaks in the injected spectra. This has been investigated in detail in

Ref. [55], where it has been also shown, however, that radio and gamma-ray data seem to favor models with no convection and with zero or very low reacceleration.

A summary of the performance of our model in fitting the various datasets that we have considered in our analysis is shown in the left panel of Fig. 9. In the plot, we compare the time-averaged sum of the time-dependent electron and positron datasets with the prediction given by the 2 breaks model. The latter is obtained by averaging over the AMS data-taking period the flux that results from solar modulation, modeled within the extension of the force-field model presented in this paper, with parameters as in Table V. Data and theoretical prediction are in remarkable agreement.

In the right panel of Fig. 9, we show the comparison between the LIS predicted by our 2 breaks model and the LIS given in Refs. [55] and [60] (for this latter case, we consider the $e^-$ LIS, as it is the only one provided in the paper). The three fluxes show a significant difference in the [100 MeV–5 GeV] energy range. As it has been illustrated in this paper, this is the domain probed mostly by radio observations and by time-dependent solar modulated fluxes. It is worth mentioning that, among the three LIS considered here, our model is the only one that is tuned on both these observations, as the LIS from Ref. [55] is not based on solar modulated data, while the model provided from Ref. [60] does not take into account radio constraints.

We hope that future studies will make use of these interstellar fluxes, which are listed in Table VI. Three applications seem most interesting and pressing. First, the inferred spectrum and charge symmetry of the extra component is tightly constrained by the measured electron flux even though it does not dominate the electron flux at any energy. Modifying the extra component would require modification of the electron spectrum at lower energies, which again is constrained by a variety of data at these energies. Therefore, the extra component can be taken as a starting point for future studies of the origin of the positron excess. Second, at the highest energies, i.e., at TeV energies and beyond, stochasticity effects due to the discrete nature of the SNRs will shape the electron spectrum (e.g., Ref. [6]). As we were mainly concerned with lower energies, we have considered a smooth distribution of sources, which produces the expectation value of the flux at any one energy. This expectation value will be most valuable when investigating the possible origin of the break observed in the all-electron spectrum around a tera-electron-volt [18,19,61]. Finally, what this study has also contributed is a new, effective way to take into account the effects of solar modulation in a time-dependent fashion. While our model has been fitted to time-dependent electron and positron fluxes above approximately 1 GeV, it should be easy to apply it to datasets extending to lower energies or the other species altogether.

## APPENDIX A: TREATMENT OF CORRELATED UNCERTAINTIES

The total uncertainty that characterizes an experimental measurement at a given energy is given by the quadratic sum of the statistical and systematic errors:

$$\sigma_{\rm tot} = \sqrt{\sigma^2_{\rm syst} + \sigma^2_{\rm stat}}. \tag{A1}$$

When dealing with datasets that extend over an extended energy range, the systematic uncertainty generally exhibits a certain degree of correlation between different energy bins. This uncertainty has to be taken into account when one is using the experimental uncertainties to compute a $\chi^2$ in order to fit the data with a given theoretical model.

The rigorous way of taking into account correlations requires the knowledge of the correlation matrix, which unfortunately is not available. Therefore, one has to resort to simpler recipes, such as the one proposed by Ref. [62]. Within such a framework, one assumes that, when computing a $\chi^2$, the systematic uncertainty of each data point is the sum of a fully correlated and a fully uncorrelated component,

$$\sigma_{\rm syst} = \sigma_{\rm syst,cor} + \sigma_{\rm syst,unc}, \tag{A2}$$

with the uncorrelated component being 1% of the measured value. Only this uncorrelated component enters the definition of the total uncertainty:

$$\sigma_{\rm tot} = \sqrt{\sigma^2_{\rm syst,unc} + \sigma^2_{\rm stat}}. \tag{A3}$$

Concerning the correlated component, it can be treated as an overall scale uncertainty on the acceptance which acts as an uncertainty on the normalization of the measured quantity. This basically means that the correlated component of the systematic uncertainty can be used to determine an uncertainty on the values of the parameters of the theoretical model that we are fitting against the data. Such uncertainty is determined by fitting the data shifted upward and downward by an amount that corresponds to the correlated uncertainty.

In the present work, we adopt the prescription described above in the fit of the CR fluxes measured by AMS. On the contrary, when we fit ratios between two CR species, we assume the correlated component of the systematic uncertainty to be negligible, i.e., $\sigma_{\rm syst} = \sigma_{\rm syst,unc}$.

## APPENDIX B: ELECTRON AND POSITRON LIS

TABLE VI. Electron and positron LIS obtained within the 2 breaks model, as described in Sec. III D. We limit the energy range to the [1 MeV–1 TeV] interval, which is the one covered by the experimental data used in our analysis.

| E (GeV) | $\Phi_{e^-}^{\rm LIS}$ (GeV m$^2$ s sr)$^{-1}$ | $\Phi_{e^+}^{\rm LIS}$ (GeV m$^2$ s sr)$^{-1}$ |
|---|---|---|
| 1.0000E − 03 | 4.0706E + 06 | 8.0054E + 01 |
| 1.2589E − 03 | 3.1598E + 06 | 6.9219E + 01 |
| 1.5849E − 03 | 2.4261E + 06 | 6.0430E + 01 |
| 1.9953E − 03 | 1.8448E + 06 | 5.3926E + 01 |
| 2.5119E − 03 | 1.3906E + 06 | 5.0008E + 01 |
| 3.1623E − 03 | 1.0393E + 06 | 4.8814E + 01 |
| 3.9811E − 03 | 7.7159E + 05 | 5.0640E + 01 |
| 5.0119E − 03 | 5.6961E + 05 | 5.6308E + 01 |
| 6.3096E − 03 | 4.1841E + 05 | 6.6900E + 01 |
| 7.9433E − 03 | 3.0593E + 05 | 8.3202E + 01 |
| 1.0000E − 02 | 2.2283E + 05 | 1.0529E + 02 |
| 1.2589E − 02 | 1.6169E + 05 | 1.3209E + 02 |
| 1.5849E − 02 | 1.1684E + 05 | 1.6068E + 02 |
| 1.9953E − 02 | 8.4072E + 04 | 1.8885E + 02 |
| 2.5119E − 02 | 6.0282E + 04 | 2.1606E + 02 |
| 3.1623E − 02 | 4.3102E + 04 | 2.4114E + 02 |
| 3.9811E − 02 | 3.0749E + 04 | 2.6021E + 02 |
| 5.0119E − 02 | 2.1907E + 04 | 2.7088E + 02 |
| 6.3096E − 02 | 1.5620E + 04 | 2.7206E + 02 |
| 7.9433E − 02 | 1.1162E + 04 | 2.6299E + 02 |
| 1.0000E − 01 | 7.9932E + 03 | 2.4085E + 02 |
| 1.2589E − 01 | 5.7282E + 03 | 2.0806E + 02 |
| 1.5849E − 01 | 4.1046E + 03 | 1.6834E + 02 |
| 1.9953E − 01 | 2.9383E + 03 | 1.2784E + 02 |
| 2.5119E − 01 | 2.0975E + 03 | 9.2251E + 01 |
| 3.1623E − 01 | 1.4856E + 03 | 6.5237E + 01 |
| 3.9811E − 01 | 1.0249E + 03 | 4.5712E + 01 |
| 5.0119E − 01 | 6.4251E + 02 | 3.1521E + 01 |
| 6.3096E − 01 | 3.9544E + 02 | 2.1044E + 01 |
| 7.9433E − 01 | 2.4154E + 02 | 1.3525E + 01 |
| 1.0000E + 00 | 1.4595E + 02 | 8.3521E + 00 |
| 1.2589E + 00 | 8.6761E + 01 | 4.9468E + 00 |
| 1.5849E + 00 | 5.0540E + 01 | 2.8252E + 00 |
| 1.9953E + 00 | 2.8794E + 01 | 1.5665E + 00 |
| 2.5119E + 00 | 1.6011E + 01 | 8.4622E − 01 |
| 3.1623E + 00 | 8.6511E + 00 | 4.4531E − 01 |
| 3.9811E + 00 | 4.5474E + 00 | 2.2935E − 01 |
| 5.0119E + 00 | 2.3168E + 00 | 1.1543E − 01 |
| 6.3096E + 00 | 1.1334E + 00 | 5.6334E − 02 |
| 7.9433E + 00 | 5.3308E − 01 | 2.6776E − 02 |
| 1.0000E + 01 | 2.4800E − 01 | 1.2782E − 02 |
| 1.2589E + 01 | 1.1509E − 01 | 6.1871E − 03 |
| 1.5849E + 01 | 5.3386E − 02 | 3.0430E − 03 |
| 1.9953E + 01 | 2.4772E − 02 | 1.5210E − 03 |
| 2.5119E + 01 | 1.1511E − 02 | 7.7192E − 04 |
| 3.1623E + 01 | 5.3631E − 03 | 3.9751E − 04 |
| 3.9811E + 01 | 2.5090E − 03 | 2.0749E − 04 |
| 5.0119E + 01 | 1.1805E − 03 | 1.0950E − 04 |
| 6.3096E + 01 | 5.5903E − 04 | 5.8203E − 05 |
| 7.9433E + 01 | 2.6692E − 04 | 3.1015E − 05 |
| 1.0000E + 02 | 1.2919E − 04 | 1.6476E − 05 |
| 1.2589E + 02 | 6.2643E − 05 | 8.6909E − 06 |
| 1.5849E + 02 | 3.0338E − 05 | 4.5425E − 06 |
| 1.9953E + 02 | 1.4669E − 05 | 2.3462E − 06 |
| 2.5119E + 02 | 7.0715E − 06 | 1.1910E − 06 |
| 3.1623E + 02 | 3.3969E − 06 | 5.9272E − 07 |
| 3.9811E + 02 | 1.6251E − 06 | 2.8800E − 07 |
| 5.0119E + 02 | 7.7325E − 07 | 1.3580E − 07 |
| 6.3096E + 02 | 3.6478E − 07 | 6.1251E − 08 |
| 7.9433E + 02 | 1.7057E − 07 | 2.6371E − 08 |
| 1.0000E + 03 | 7.9074E − 08 | 1.0779E − 08 |


[1] A. D. Panov *et al.*, Bull. Russ. Acad. Sci. Phys. **73**, 564 (2009).
[2] Y. S. Yoon *et al.*, Astrophys. J. **728**, 122 (2011).
[3] O. Adriani *et al.* (PAMELA Collaboration), Science **332**, 69 (2011).
[4] M. Aguilar *et al.* (AMS Collaboration), Phys. Rev. Lett. **114**, 171103 (2015).
[5] M. Aguilar *et al.* (AMS Collaboration), Phys. Rev. Lett. **115**, 211101 (2015).
[6] P. Mertsch, J. Cosmol. Astropart. Phys. 11 (2018) 045.
[7] M. A. DuVernois *et al.*, Astrophys. J. **559**, 296 (2001).
[8] S. Coutu *et al.*, Astropart. Phys. **11**, 429 (1999).
[9] O. Adriani *et al.* (PAMELA Collaboration), Nature (London) **458**, 607 (2009).

[10] D. Hooper, P. Blasi, and P. D. Serpico, J. Cosmol. Astropart. Phys. 01 (2009) 025.
[11] S. Profumo, Central Eur. J. Phys. **10**, 1 (2011).
[12] P. Blasi, Phys. Rev. Lett. **103**, 051104 (2009).
[13] M. Ahlers, P. Mertsch, and S. Sarkar, Phys. Rev. D **80**, 123017 (2009).
[14] M. Cirelli, M. Kadastik, M. Raidal, and A. Strumia, Nucl. Phys. **B813**, 1 (2009); **B873**, 530(A) (2013).
[15] I. Cholis, L. Goodenough, D. Hooper, M. Simet, and N. Weiner, Phys. Rev. D **80**, 123511 (2009).
[16] M. Boudaud *et al.*, Astron. Astrophys. **575**, A67 (2015).
[17] F. Aharonian *et al.* (H.E.S.S. Collaboration), Phys. Rev. Lett. **101**, 261104 (2008).
[18] F. Aharonian *et al.* (H.E.S.S. Collaboration), Astron. Astrophys. **508**, 561 (2009).
[19] G. Ambrosi *et al.* (DAMPE Collaboration), Nature (London) **552**, 63 (2017).
[20] M. Aguilar *et al.* (AMS Collaboration), Phys. Rev. Lett. **122**, 041102 (2019).
[21] M. S. Potgieter, Living Rev. Solar Phys. **10**, 3 (2013).
[22] O. Adriani *et al.*, Astrophys. J. **810**, 142 (2015).
[23] O. Adriani *et al.* (PAMELA Collaboration), Phys. Rev. Lett. **116**, 241105 (2016).
[24] M. Aguilar *et al.* (AMS Collaboration), Phys. Rev. Lett. **121**, 051102 (2018).
[25] A. C. Cummings, E. C. Stone, B. C. Heikkila, N. Lal, W. R. Webber, G. Jóhannesson, I. V. Moskalenko, E. Orlando, and T. A. Porter, Astrophys. J. **831**, 18 (2016).
[26] K. M. Ferrière, Rev. Mod. Phys. **73**, 1031 (2001).
[27] D. R. Lorimer *et al.*, Mon. Not. R. Astron. Soc. **372**, 777 (2006).
[28] G. L. Case and D. Bhattacharya, Astrophys. J. **504**, 761 (1998).
[29] T. Kamae, T. Abe, and T. Koi, Astrophys. J. **620**, 244 (2005).
[30] T. Kamae, N. Karlsson, T. Mizuno, T. Abe, and T. Koi, Astrophys. J. **647**, 692 (2006); **662**, 779(E) (2007).
[31] J. W. Norbury and L. W. Townsend, Nucl. Instrum. Methods Phys. Res., Sect. B **254**, 187 (2007).
[32] A. W. Strong, I. V. Moskalenko, and O. Reimer, Astrophys. J. **613**, 962 (2004).
[33] V. L. Ginzburg and S. I. Syrovatskii, *The Origin of Cosmic Rays, New York: Macmillan, 1964* (Pergamon Press, Oxford, 1964).
[34] V. S. Berezinskii, S. V. Bulanov, V. A. Dogiel, and V. S. Ptuskin, *Astrophysics of Cosmic Rays*, edited by V. L. Ginzburg (North-Holland, Amsterdam, 1990).
[35] C. Evoli, D. Gaggero, D. Grasso, and L. Maccione, J. Cosmol. Astropart. Phys. 10 (**2008**) 018; 04 (2016) E01.
[36] C. Evoli, D. Gaggero, A. Vittino, G. Di Bernardo, M. Di Mauro, A. Ligorini, P. Ullio, and D. Grasso, J. Cosmol. Astropart. Phys. 02 (2017) 015.
[37] M. S. Pshirkov, P. G. Tinyakov, P. P. Kronberg, and K. J. Newton-McGee, Astrophys. J. **738**, 192 (2011).
[38] A. W. Strong, I. V. Moskalenko, and O. Reimer, Astrophys. J. **537**, 763 (2000); **541**, 1109(E) (2000).
[39] T. A. Porter and A. W. Strong, in *Proceedings, 29th International Cosmic Ray Conference (ICRC 2005): Pune, India, 2005* (Tata Institute of Fundamental Research, Mumbai, India, 2005), Vol. 4, pp. 77–80.
[40] V. S. Ptuskin, I. V. Moskalenko, F. C. Jones, A. W. Strong, and V. N. Zirakashvili, Astrophys. J. **642**, 902 (2006).
[41] M. Aguilar *et al.* (AMS Collaboration), Phys. Rev. Lett. **120**, 021101 (2018).
[42] M. Aguilar *et al.* (AMS Collaboration), Phys. Rev. Lett. **119**, 251101 (2017).
[43] P. Blasi, E. Amato, and P. D. Serpico, Phys. Rev. Lett. **109**, 061101 (2012).
[44] E. N. Parker, Planet. Space Sci. **13**, 9 (1965).
[45] L. J. Gleeson and W. I. Axford, Astrophys. J. **154**, 1011 (1968).
[46] A. Gruzinov, arXiv:1808.00041.
[47] W. H. Matthaeus, S. Dasso, J. M. Weygand, L. J. Milano, C. W. Smith, and M. G. Kivelson, Phys. Rev. Lett. **95**, 231101 (2005).
[48] W. H. Matthaeus, G. P. Zank, C. W. Smith, and S. Oughton, Phys. Rev. Lett. **82**, 3444 (1999).
[49] A. Teufel and R. Schlickeiser, Astron. Astrophys. **397**, 15 (2003).
[50] G. Di Bernardo, C. Evoli, D. Gaggero, D. Grasso, and L. Maccione, J. Cosmol. Astropart. Phys. 03 (2013) 036.
[51] M. Aguilar *et al.* (AMS Collaboration), Phys. Rev. Lett. **113**, 121102 (2014).
[52] T. R. Jaffe, A. J. Banday, J. P. Leahy, S. Leach, and A. W. Strong, Mon. Not. R. Astron. Soc. **416**, 1152 (2011).
[53] A. W. Strong, E. Orlando, and T. R. Jaffe, Astron. Astrophys. **534**, A54 (2011).
[54] E. Orlando and A. Strong, Mon. Not. R. Astron. Soc. **436**, 2127 (2013).
[55] E. Orlando, Mon. Not. R. Astron. Soc. **475**, 2724 (2018).
[56] G. Hinshaw *et al.*, Astrophys. J. Suppl. Ser. **208**, 19 (2013).
[57] A. Cheminet, G. Hubert, V. Lacoste, D. Maurin, and L. Derome, J. Geophys. Res. Space Physics **118**, 7488 (2013).
[58] R. D. Strauss, M. S. Potgieter, I. Büsching, and A. Kopp, Astrophys. Space Sci. **339**, 223 (2012).
[59] R. Munini *et al.*, Proc. Sci., ICRC2017 (**2018**) 012.
[60] M. S. Potgieter and E. E. Vos, Astron. Asprophys. **601**, A23 (2017).
[61] D. Kerszberg, M. Kraus, D. Kolitzus, K. Egberts, S. Funk, J.-P. Lenain, O. Reimer, P. Vincent (H.E.S.S. Collaboration), *Proceedings of the 35th International Cosmic Ray Conference, Busan, Korea* (2017), https://indico.snu.ac.kr/indico/event/15/session/5/contribution/694.
[62] L. A. Cavasonza, H. Gast, M. Krämer, M. Pellen, and S. Schael, Astrophys. J. **839**, 36 (2017).